Available online at www.sciencedirect.com
SCIENCE DIRECT
Earth and Planetary Science Letters 246 (2006) 326–335
EPSL
www.elsevier.com/locate/epsl

Stability and compressibility of the high-pressure phases of Al_2O_3 up to 200 GPa: Implications for the electrical conductivity of the base of the lower mantle

Shigeaki Ono [a,*], Artem R. Oganov [b], Takao Koyama [c], Hisayoshi Shimizu [c]

[a] *Institute for Research on Earth Evolution, Japan Agency for Marine-Earth Science and Technology, 2-15 Natsushima-cho, Yokosuka-shi, Kanagawa 237-0061, Japan*
[b] *Laboratory of Crystallography, Department of Materials, ETH Hönggerberg, Wolfgang-Pauli-Strasse 10, CH-8093 Zurich, Switzerland*
[c] *Earthquake Research Institute, University of Tokyo, 1-1-1 Yayoi, Bunkyo-ku, Tokyo 113-0032, Japan*

Received 25 November 2005; received in revised form 7 April 2006; accepted 9 April 2006
Available online 24 May 2006
Editor: G.D. Price

Abstract

We have used a laser-heated diamond anvil cell to investigate the stability and compressibility of *Cmcm* $CaIrO_3$-type (post-perovskite structure) Al_2O_3 at pressures up to 200 GPa. A phase transformation from the *Pbcn* Rh_2O_3(II)-type to the $CaIrO_3$-type structure was observed at 130 GPa, which is consistent with previous theoretical studies. The observed $CaIrO_3$-type structure in Al_2O_3 is the same as that in $MgSiO_3$ post-perovskite, the main mineral of Earth's lowermost mantle. We also calculated the Raman shifts of $CaIrO_3$-type Al_2O_3 and $MgSiO_3$ using density-functional perturbation theory. The similarity of the crystal structures and Raman spectra of $CaIrO_3$-type Al_2O_3 and $MgSiO_3$ suggests that the other physical properties of the two phases could be similar as well. Based on the high electrical conductivity of $CaIrO_3$-type Al_2O_3, we predicted a profile of electrical conductivity at the bottom of the lower mantle, which can explain Earth's rotation period changes of a few milliseconds in Earth's length of day on decadal timescales, if the exchange of angular momentum between the solid mantle and fluid core occurs by an electromagnetic coupling between the conducting core and mantle.

Keywords: phase transition; Al_2O_3; electrical conductivity; lower mantle; Alumina; Raman shift; high pressure

1. Introduction

The structural and electronic properties of alumina are of considerable importance due to the diverse applications of this material, particularly in high-pressure science. It is used as a window material in shock-wave experiments, and the Cr^{3+}-doped form called ruby, serves as a pressure standard in diamond anvil cell experiments, through measurement of the pressure-dependent shift of its fluorescence lines. Alumina, in common with a range of A_2O_3 oxides, crystallizes under ambient conditions into the corundum structure with space group *R-3c*, in which all the cations are in a six-coordinate state. On increasing pressure, some A_2O_3 compounds transform into a Rh_2O_3 (II)-type structure with space group *Pbcn*. For Al_2O_3, the Rh_2O_3(II)-type structure has been reported in both

* Corresponding author. Tel.: +81 468 67 9763; fax: +81 468 67 9625.
E-mail address: sono@jamstec.go.jp (S. Ono).

0012-821X/$ - see front matter © 2006 Elsevier B.V. All rights reserved.
doi:10.1016/j.epsl.2006.04.017

theoretical and experimental studies [e.g., 1–6]. Some theoretical studies have also predicted that Al_2O_3 can further transform into a perovskite structure with space group *Pbnm* at pressures above 200 GPa [2,6,7]. Recently, Oganov and Ono [8] synthesized $CaIrO_3$-type (post-perovskite structure) Al_2O_3 with space group *Cmcm* in high-pressure experiments. First-principle calculations also showed that $CaIrO_3$-type Al_2O_3 is stable at high pressures when compared to the perovskite structure [8–10]. However, the stability and physical properties of $CaIrO_3$-type Al_2O_3 have not been investigated in high-pressure experiments.

Although Earth's rotation period changes over different timescales, changes occurring over several years and also over very long timescales can be explained by changes in Earth's moment of inertia due to a coupling between the atmosphere and oceans and the tidal friction, respectively [11]. Measured changes of a few milliseconds in Earth's length of day on decadal timescales are attributed to the exchange of angular momentum between the solid mantle and fluid core. A review of core–mantle coupling and angular momentum exchange has been published by Bloxham [12]. To explain the length-of-day type of variations on decadal timescales, the following mechanisms have been proposed: (1) gravitational coupling between changes in density and/or topographic inhomogeneities of the inner core and mantle [13,14], (2) topographic coupling from fluid pressure on the deformed core–mantle boundary [15–17], and (3) electromagnetic coupling between the core and a weakly conducting mantle [18–22].

Although the third mechanism can reasonably explain the observed changes of a few milliseconds in Earth's length of day on decadal timescales, this mechanism requires a highly conductive layer at the base of the lower mantle. However, it is known that magnesium silicate perovskite, which is the dominant mineral in the lower mantle, does not have such a high electrical conductivity [23,24]. Even if molten iron, which has a high electrical conductivity, can penetrate from the outer core into the solid mantle, the depth of penetration of molten iron into the solid mantle would be short [25]. This indicates that the enhancement of the electrical conductivity of the solid mantle by penetration of molten iron would not be enough to explain the electromagnetic coupling between the core and the mantle.

Therefore, this mechanism was considered unrealistic if the lowermost part of the lower mantle is composed

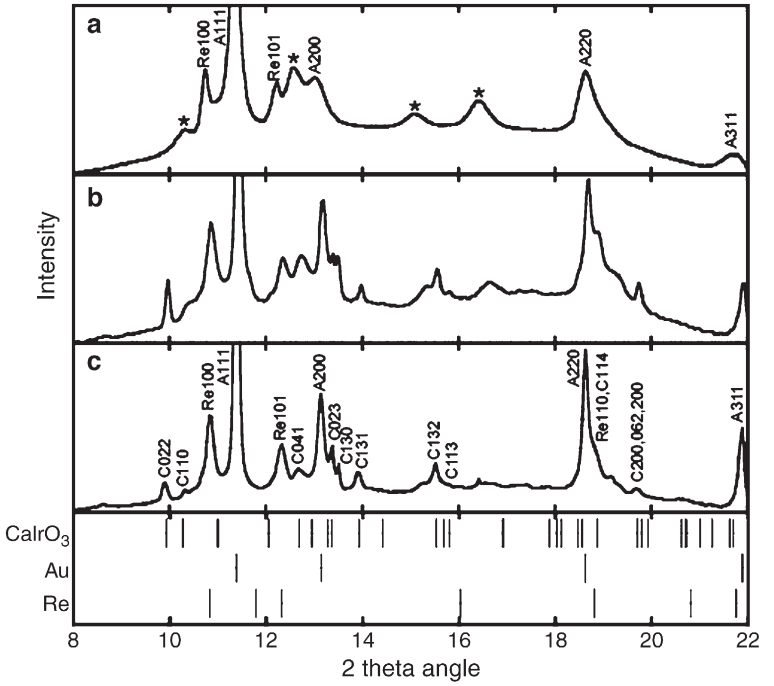

Fig. 1. Examples of diffraction patterns of $CaIrO_3$-type Al_2O_3. These diffraction patterns were obtained at a pressure of about 150 GPa. a, Before the laser heating at 300 K; b, during the heating at about 2000 K; c, after the temperature quench. Abbreviations for peaks are as follows: C, $CaIrO_3$-type Al_2O_3; A, gold; Re, rhenium gasket. The stars denote the broad peaks of the starting material. The vertical bars denote the calculated positions of the diffraction lines of each phase. The unit cell dimensions are $CaIrO_3$-type Al_2O_3, $a=2.4307$ Å, $b=7.925$ Å, $c=6.053$ Å; gold, $a=3.634$ Å; and rhenium, $a=2.546$ Å, $c=4.051$ Å. The wavelength of the monochromatic incident X-ray beam was 0.4159 Å.

only of magnesium silicate perovskite. Buffett [26] also discussed the possibility that a high electrical conductive layer may exist at the core–mantle boundary region after observing periodic variations (nutation) in Earth's rotation. Although Buffett et al. [27] argued the possibility that the sedimentation at the top of the outer core forms a layer of high electrical conductivity, there is no experimental evidence that supports this assertion.

Recently, the possibility of $CaIrO_3$-type Al_2O_3 with high electrical conductivity has been reported [8]. First principle studies show that $CaIrO_3$-type $MgSiO_3$ phase, which is likely to have analogous high electrical conductivity, can exist at the base of the lower mantle [e.g., 28,29]. The possibility of a highly conductive D″ layer requires a reappraisal of the electromagnetic coupling mechanism to understand the observed changes in Earth's length of day.

We used a laser-heated diamond anvil cell (DAC) and intense X-rays from a synchrotron radiation source to acquire precise data on Al_2O_3 under high pressure, and directly observed a phase transformation between Rh_2O_3(II)-type and $CaIrO_3$-type Al_2O_3. We also investigated the pressure–volume equation of state (EOS) of $CaIrO_3$-type Al_2O_3 over the pressure range 120 to 180 GPa. Ab initio calculations were performed to investigate the Raman shifts of the $CaIrO_3$-type phases at high pressure, and we investigated the similarities in physical properties between $CaIrO_3$-type Al_2O_3 and $MgSiO_3$ based on experimental and theoretical data. This allowed us to estimate the profile of the electrical conductivity at the bottom of the lower mantle.

2. Methods

2.1. High-pressure experiments

Powdered Al_2O_3 corundum was used as the starting material. Gold powder was mixed with the sample to absorb the laser radiation for efficient laser heating and for use as an internal pressure calibrant. Gel-type $MgSiO_3$ powder was also used to investigate the similarities in physical properties between Al_2O_3 and $MgSiO_3$. The powders were comminuted in an agate mortar to ensure homogeneity and a small grain size. High-pressure X-ray diffraction experiments were performed in a laser-heated symmetric-type diamond anvil cell with a 60° conical aperture [30]. The diamonds had an inner culet of 100 μm and an outer culet of 600 μm,

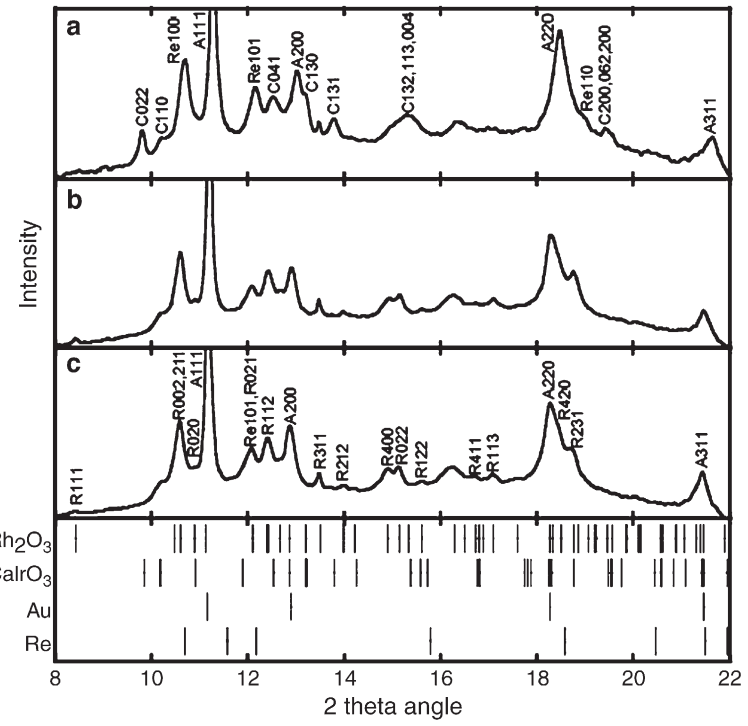

Fig. 2. The phase transition from Rh_2O_3(II)-to $CaIrO_3$-type Al_2O_3. a, Before the laser heating; b, on heating; c, after the temperature quench. Abbreviations for peaks are as follows: R, Rh_2O_3(II)-type Al_2O_3; C, $CaIrO_3$-type Al_2O_3; A, gold; and Re, rhenium gasket. The vertical bars denote the calculated positions of the diffraction lines of each phase. The unit cell dimensions are Rh_2O_3(II)-type Al_2O_3, a=6.412 Å, b=4.380 Å, c=4.551 Å; $CaIrO_3$-type Al_2O_3, a=2.449 Å, b=8.029 Å, c=6.082 Å; gold, a=3.703 Å; and rhenium, a=2.564 Å, c=4330 Å.

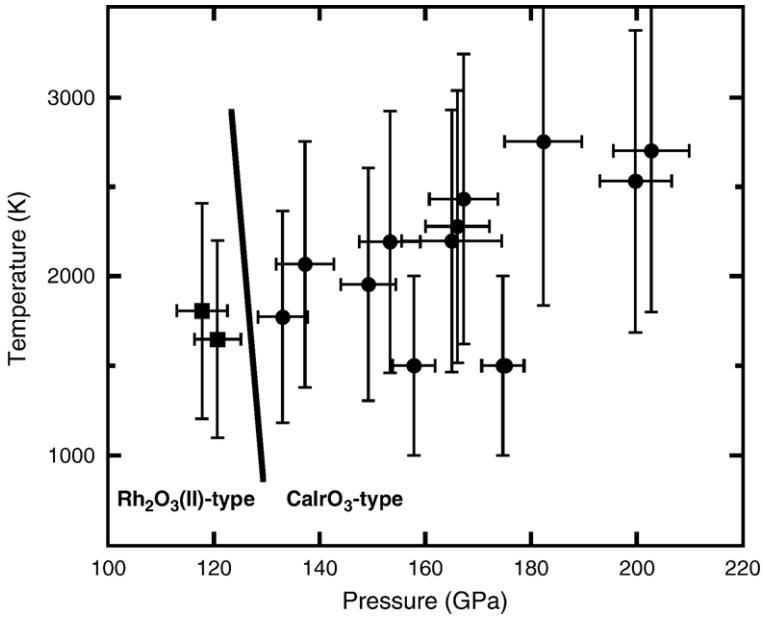

Fig. 3. Experimental results and the phase boundary determined from in situ X-ray observations. Solid squares and circles denote conditions where Rh_2O_3(II)-type and $CaIrO_3$-type Al_2O_3 were stable. The error bars in pressure include the uncertainty of at temperature, because the EOS is used to calculate the sample pressure. The thick line denotes the inferred phase boundary between the two high-pressure phases. The gradient of dP/dT of this phase boundary was reported by a theoretical study [8].

with a beveled angle of 17°. The powdered sample was loaded into a 40 μm diameter hole drilled into a rhenium gasket, and no pressure-transmitting medium was used. The samples were heated with either a YLF or YAG laser to overcome any potential kinetic effect on the phase transition. The size of the heated spot was 20–30 μm.

The sample was initially compressed to the desired pressure at room temperature, and then the load on the DAC was kept constant during laser heating. After being kept at the desired pressure and temperature for a given period, the sample was quenched by shutting off the laser. The sample temperature was measured using the spectroradiometric method [31]. The spectroradiometric system consisted of a thermoelectrically cooled CCD detector and a spectrograph. The use of the spectrometer allowed us to measure the temperature profile across the laser-heated spot. The temperature was determined by fitting the thermal radiation spectrum between $\lambda = 600$ and 800 nm to the Planck radiation function [e.g., 31–33]. The system response was calibrated using a tungsten filament lamp of known radiance that was calibrated relative to an NIST standard. The heated samples were probed using angle-dispersive X-ray diffraction using at the monochromatic incident X-ray synchrotron beam lines BL10XU, SPring-8 [34], and BL13A, Photon Factory [35] in Japan. The X-ray beams were collimated to a diameter of 10–20 μm, and the angle-dispersive X-ray diffraction patterns were obtained on an imaging plate or on an X-ray CCD detector. The detector-to-sample distances were calibrated using a standard CeO_2. The uncertainties of the distances were <0.1%. The observed intensities on the imaging plates were integrated as a function of 2θ using the ESRF Fit2d software code [36] to obtain one-dimensional diffraction profiles. The diffraction peak positions were determined using a peak-fitting program. The pressure was estimated from the observed unit cell volumes

Table 1
Lattice parameters and volumes of Al_2O_3 phases at 300 K

P (GPa)	a (Å)	b (Å)	c (Å)	Volume (Å^3)
Rh_2O_3(II)				
102.8(11)	6.412(5)	4.380(5)	4.551(4)	127.79(21)
$CaIrO_3$				
124.0(4)	2.449(5)	8.029(16)	6.082(12)	119.59(41)
137.9(6)	2.423(7)	7.965(23)	6.053(43)	116.82(96)
140.8(7)	2.431(1)	7.925(6)	6.053(5)	116.60(14)
148.4(8)	2.425(2)	7.908(12)	6.001(15)	115.11(35)
163.3(17)	2.406(2)	7.936(8)	6.014(6)	113.38(17)
166.5(10)	2.407(2)	7.843(9)	5.989(7)	113.06(20)
181.4(9)	2.389(2)	7.821(8)	5.936(8)	110.87(22)

Numbers in parentheses represent the error of lattice parameter and volume of Al_2O_3 phases. Pressures were determined from the observed unit cell volume of gold using the gold equation of state [37].

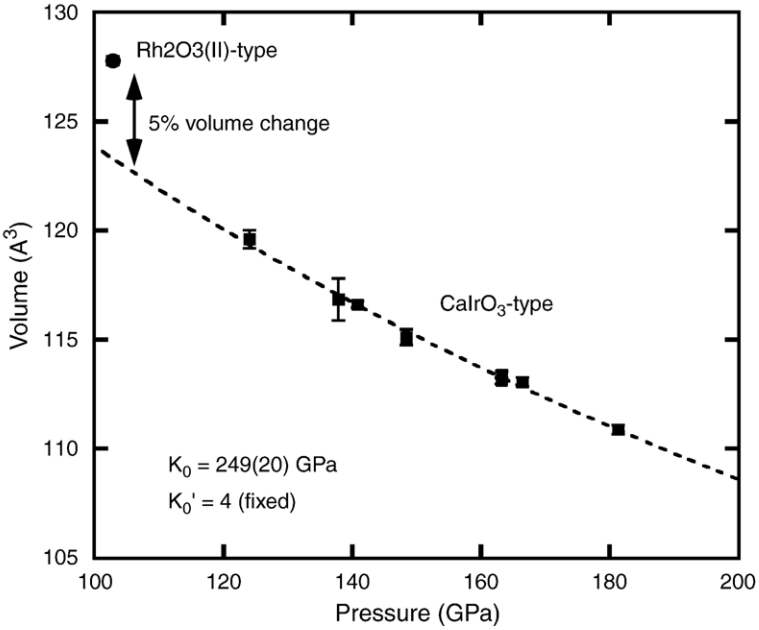

Fig. 4. Pressure–volume data for Al_2O_3 high-pressure phases at 300 K. The solid circle and squares denote the volume data of Rh_2O_3(II)-type and $CaIrO_3$-type Al_2O_3, respectively. The dashed curve is the third-order Birch–Murnaghan equation fit with parameters K_0=249 GPa and K_0'=4 using Jamieson's EOS of Au.

using the equation of state (EOS) of gold [37]. Because we used the EOS, the uncertainty in the pressure was dependent on the experimental temperature. The temperature error at high temperatures was greater than 500 K. The estimated pressure errors at high temperatures included the uncertainty of temperature in the sample.

2.2. Theoretical calculations

We performed calculations based on the plane wave pseudopotential methodology and the local density approximation (LDA), as implemented in the ABINIT code [38], a common project of the Université Catholique de Louvain, Corning Inc., and other contributors (URL http://www.abinit.org). Non-local Troullier–Martins pseudopotentials [39] with partial core corrections [40] were used. A plane wave kinetic energy cut-off of 45 Ha and 6×6×4 Monkhorst–Pack meshes for the Brillouin zone were used, and produced highly converged results. Primitive 10-atom cells were used in all the calculations. $CaIrO_3$-type Al_2O_3 and $MgSiO_3$ were optimized at 130 GPa using the steepest-descent method. For more technical details on the pseudopotentials and convergence tests, see Oganov and Ono [8,29]. The phonon frequencies were computed at the Γ-point for the optimized structures using density-functional perturbation theory [41–43]. From group-theoretical considerations, we found that twelve modes in the Brillouin zone centre ware Raman-active ($4A_g+3B_{1g}+B_{2g}+4B_{3g}$).

3. Results

The in situ high-pressure and high-temperature X-ray diffraction patterns are shown in Fig. 1. The pressure was increased directly to about 150 GPa at room temperature, and an X-ray diffraction pattern of the sample was recorded. A strain-broadening of the diffraction peaks of the starting material was observed, because a large differential stress was induced in the diamond anvil cell as the pressure increased. However, no phase transition from corundum to a high-pressure phase was observed (Fig. 1a). Next, the sample was

Table 2
Comparison of the bulk modulus of $CaIrO_3$-type Al_2O_3

	K_0 (GPa)	K_0'	V_0 (Å^3)
Theoretical			
Oganov and Ono [8]	241.6	4.464	161.17
Caracas and Cohen [9]	231	4.38	155.12
Experimental			
This study	249(20)	4 (fixed)	158.4(26)

V_0, K_0, and K_0' are the volume, the isothermal bulk modulus, and the first pressure derivative of the isothermal bulk modulus, respectively. Experimental data were acquired at 300 K.

Table 3
Comparison of X-ray diffraction patterns of $CaIrO_3$-type Al_2O_3 and $MgSiO_3$

hkl	Al_2O_3					$MgSiO_3$			
	d_{obs}, Å	d_{cal}, Å	$d_{obs}/d_{cal}-1$	I_{obs}	I_{cal}	d_{obs},Å	d_{cal},Å	$d_{obs}/d_{cal}-1$	I_{obs}
020		3.9296			<1		4.0173		
002		2.9950			1		3.0408		
022	2.3876	2.3876	0.0023	100	100	2.4241	2.4246	−0.0002	43
110	2.2951	2.2951	−0.0011	17	21	2.3473	2.3475	−0.0001	6
111	*				4	2.1874	2.1900	−0.0012	1
040	1.9567	1.9567	−0.0041	6	4		2.0087		
041	1.8664	1.8664	−0.0003	20	9	1.9028	1.9073	−0.0024	6
023	1.7842	1.7801	0.0023	36	48	1.8102	1.8098	0.0002	100
130	1.7715	1.7706	0.0005	67	74	1.8102	1.8096	0.0004	100
131	1.6979	1.6980	−0.0001	78	100	1.7348	1.7344	0.0002	54
042		1.6428			1	1.6736	1.6760	−0.0014	4
132	1.5263	1.5242	0.0014	62	64	1.5552	1.5550	0.0001	23
113	1.5073	1.5071	0.0001	32	53	1.5366	1.5343	0.0015	23
004	1.4945	1.4975	−0.0020	14	30	1.5206	1.5204	0.0001	14
133	1.3252	1.3252	0.0003	6	19	1.3485	1.3500	−0.0011	5
150		1.3153			3		1.3391		
151	1.2833	1.2847	−0.0011	13	22	1.3133	1.3128	0.0004	13
114	*	1.2545			29	*	1.2761		
152		1.2043			27	1.2277	1.2296	−0.0016	17
200	1.2012	1.2001	0.0009	42	31	1.2277	1.2273	0.0003	17
062	1.2012	1.2012	0.0000	42	44	1.2277	1.2255	0.0017	17

Calculated d-spacings of Al_2O_3 and $MgSiO_3$ phases are based on orthorhombic unit cell dimensions of $a=2.402(2)$ Å, $b=7.859(6)$ Å, $c=5.990(6)$ Å and $a=2.455(2)$ Å, $b=8.035(6)$ Å, $c=6.082(6)$ Å. Wyckoff symbols and positions of each atom in calculated $CaIrO_3$-type Al_2O_3; Al1, 4a, (0, 0, 0); Al2, 4c, (0, 0.2514, 0.25); O1, 4c, (0, 0.9092, 0.25); O2, 8f, (0, 0.6448, 0.4289). *Peaks are overlapped by those of gold and rhenium.

heated to 1500–2500 K to relax the differential stress and to overcome potential kinetic effects on the possible phase transition. Many new peaks appeared in the diffraction pattern during heating (Fig. 1b). Thus, the corundum starting material was transformed into a new high-pressure phase. After heating, the diffraction patterns showed no extra change. This implies that the new high-pressure phase can be temperature-quenched (Fig. 1c). The new phase was reasonably indexed to an orthorhombic cell with four formula units ($Z=4$). The space group of this phase was consistent with the *Cmcm* symmetry, which is adopted by $CaIrO_3$-type Al_2O_3 [8]. The $CaIrO_3$-type phase was not pressure-quenchable because only the X-ray diffraction pattern of corundum was observed after decompression to ambient pressure.

In the next run, the pressure and temperature of the sample were varied to investigate the stability of the $CaIrO_3$-type phase after synthesis. During decompression, the $CaIrO_3$-type phase was stable at pressures higher than 130 GPa. However, the phase transition from the $CaIrO_3$-type to the Rh_2O_3(II)-type phase was observed below 130 GPa. Fig. 2 shows changes in the X-ray diffraction patterns during this phase transition. Before heating, the X-ray diffraction pattern of the $CaIrO_3$-type phase was observed (Fig. 2a). A change in the diffraction pattern was observed during heating (Fig. 2b). The diffraction peaks of the $CaIrO_3$-type phase disappeared, and new peaks were observed. These new peaks remained after the temperature quenching (Fig. 2c). The new peaks were indexed based on an Rh_2O_3 (II)-type structure.

The phases observed in this study are shown in Fig. 3. The $CaIrO_3$-type phase was stable up to 200 GPa. The phase boundary between the Rh_2O_3(II)-type phase and

Table 4
Comparison of the calculated Raman frequencies (cm^{-1}) of the $CaIrO_3$-type phases of Al_2O_3 and $MgSiO_3$ at 130 GPa

Mode	$MgSiO_3$	Al_2O_3
A_g	474.12	472.96
A_g	587.58	730.11
A_g	889.60	883.89
A_g	998.17	984.65
B_{1g}	373.53	345.74
B_{1g}	627.72	807.73
B_{1g}	787.87	661.63
B_{2g}	742.78	719.80
B_{3g}	531.15	378.96
B_{3g}	606.96	646.38
B_{3g}	929.65	892.11
B_{3g}	1161.64	1065.88

the $CaIrO_3$-type phase is located at about 130 GPa. The boundary determined in this study is in good agreement with that calculated theoretically [8]. Caracas and Cohen [9] reported a theoretical phase boundary at 156 GPa at 0 K, whereas Tsuchiya et al. [10] found a transition pressure of 150–172 GPa at 0 K. These values are somewhat higher than our experimental data. Lin et al. [5] reported that the Rh_2O_3(II)-type Al_2O_3 (doped with Cr^{3+}) remained stable up to 136 GPa and 2350 K. The stability field of the Rh_2O_3(II)-type phase observed in their study was stable at slightly higher pressures than those observed in our study. As our experimental uncertainty was large under extreme high-pressure conditions, this discrepancy is likely to be insignificant.

Table 1 shows the cell parameters and volumes of the observed phases. As can be seen in Fig. 4, a discontinuity in the volume between the Rh_2O_3(II)-type phase and the $CaIrO_3$-type phase indicates that this is a first-order phase transition, with a relative volume change of about 5%. A refinement of the volume data of the $CaIrO_3$-type phase yields the third-order Birch–Murnaghan equations of state parameters. The bulk modulus, K_0, was 249(±20) GPa and the volume, V_0, was 158.4(±2.6) $Å^3$ when the first pressure derivative of the bulk modulus, K_0', is fixed at $K_0'=4$. A comparison of the elastic parameters between theoretical studies and our experimental observations are shown in Table 2. The experimental values are in good agreement with those of theoretical studies.

4. Discussion

4.1. Similarities between $CaIrO_3$-type Al_2O_3 and $MgSiO_3$

Previous high-pressure studies have shown that high-pressure phases of $MgSiO_3$ form solid solutions with Fe_2O_3 and Al_2O_3. McCammon [44], and Frost et al. [45] have reported that a significant amount of Fe_2O_3 dissolves into $MgSiO_3$ perovskite. An incorporation of Al_2O_3 into $MgSiO_3$ perovskite has also been reported [46]. The solubility of these components is facilitated by the structural similarities between Fe_2O_3, $MgSiO_3$, and Al_2O_3. From the viewpoint of the similarity in the sequence of pressure-induced phase transitions, Fe_2O_3, Al_2O_3, and $MgSiO_3$ transform into a $CaIrO_3$-type

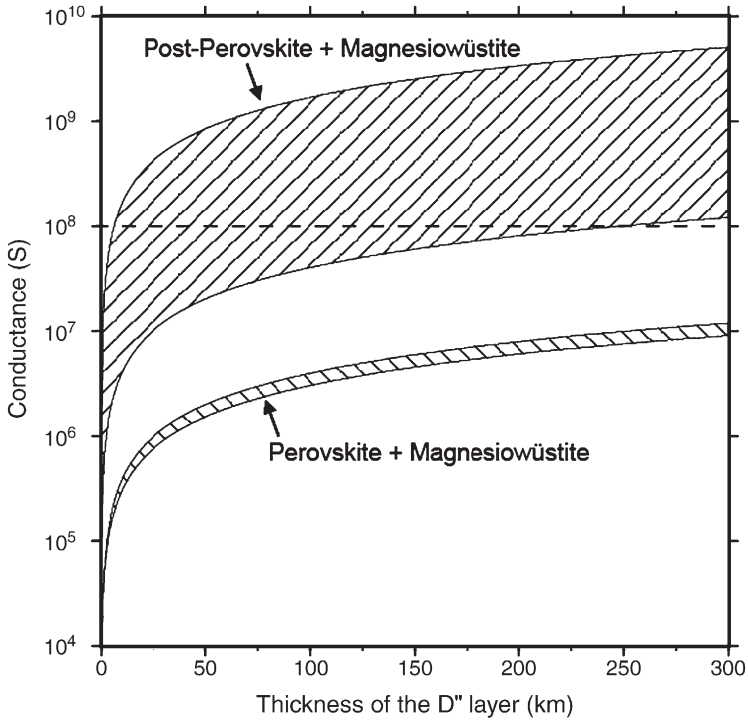

Fig. 5. Electrical conductivity of perovskite+magnesiowustite, and $CaIrO_3$-type phase+magnesiowustite rocks. The electrical conductivity of $CaIrO_3$-type (post-perovskite) $MgSiO_3$ was assumed to be one to two orders of magnitude higher than that of $MgSiO_3$ perovskite. The shaded denote the area between the upper and lower bounds of the two-phase materials [51]. If the conductance is $>10^8$ S/m, which is a product of the electrical conductivity and the thickness of the conductive layer, then the decadal variation of the length of day can be explained by an advective electromagnetic toroidal torque [21].

structure at high pressures. Similarities between these isostructural phases are important for understanding the physical properties of Earth's lowermost mantle, the mineralogy of which is dominated by $CaIrO_3$-type $MgSiO_3$.

Table 3 shows a comparison of the observed X-ray diffraction patterns of $CaIrO_3$-type Al_2O_3 and $MgSiO_3$. The cell parameters and peak intensities of Al_2O_3 are similar to those of $MgSiO_3$. Although it is difficult to determine the atomic positions of both phases using experimental data, the similarity in cell parameters and peak intensities indicates that the atomic positions are nearly the same. The lower limit of the stability field of $CaIrO_3$-type Al_2O_3 is almost the same as that of $MgSiO_3$. These simple observations strengthen the analogy between the two materials, which is further supported by the similarity of their Raman frequencies.

Table 4 shows the calculated Raman frequencies of these phases at 130 GPa and their symmetry assignments. It can be seen that in most cases, the agreement between the frequencies was within 10%. This, in turn, implies that the strength of the interatomic interactions (and hence, many other properties) between the two materials is not dissimilar. Since Raman spectroscopy is one of the most convenient probes of matter at ultrahigh pressures, the data in Table 4 can be used to identify $CaIrO_3$-type Al_2O_3 and $MgSiO_3$.

4.2. Electrical conductivity of the D″ layer

As Earth's mantle consists of elements in addition to Mg, Si, Fe, and O, knowing the effect of minor elements is important in understanding the physics and chemistry of Earth's lower mantle. For example, Xu et al. [24] reported that incorporation of Al_2O_3 increases the electrical conductivity of $MgSiO_3$ perovskite. Recently, Oganov and Ono [8] hypothesized that the electrical conductivity of the D″ layer was much higher than that of other parts of Earth's mantle, because the $CaIrO_3$-type (post-perovskite structure) Al_2O_3 has a high conductivity, and the D″ layer consists of isostructural $CaIrO_3$-type $MgSiO_3$. On the other hand, observations of changes in Earth's rotation period imply that there is the possibility of the existence of a highly conducting layer at the base of the lower mantle [e.g., 20,21]. Therefore, we assessed the highly conductive layer model predicted by observations on changes in Earth's rotation period.

Fig. 5 shows the relationship between the conductivity predicted by the observations on changes in

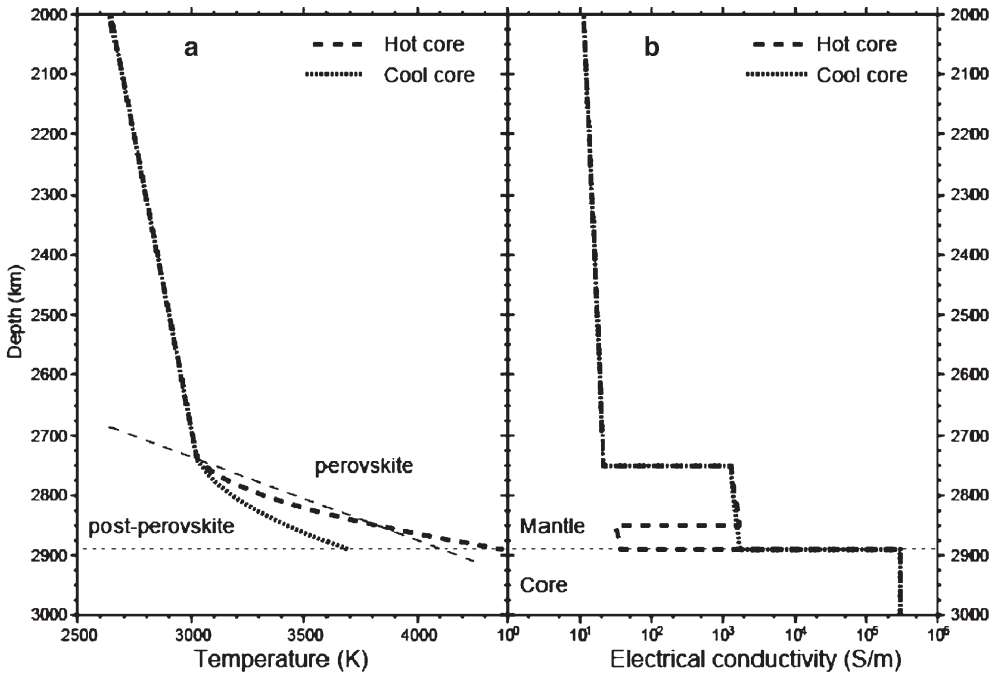

Fig. 6. Temperature and electrical conductivity profiles in the lowermost mantle. a, The temperature models used to estimate the conductivity profile were taken from Hernlund et al. [49]. b, The electrical conductivity model derived from the perovskite, $CaIrO_3$-type (post-perovskite) phase, and magnesiowustite [47], were estimated using the effective medium theory [52]. The electrical conductivity of the $CaIrO_3$-type phase was assumed to be two orders of magnitude higher than that of perovskite.

Earth's rotation and the conductivity of mantle rock estimated from mineral physics. Holme [21] suggested the conductance of the highly conductive layer was $>10^8$ S. The conductance depends on the electrical conductivity of the rock and the layer thickness. If the conductive layer corresponds to the D″ layer, then the layer thickness is 100–300 km. Xu et al. [47] estimated that the electrical conductivity of perovskite-bearing rock is $10–10^2$ S/m, but the electromagnetic coupling model cannot explain the conductance of deep mantle based on perovskite-bearing rock [21].

Since the electrical conductivity of $CaIrO_3$-type $MgSiO_3$ has not been measured, we have to rely on the analogy between $MgSiO_3$ and Al_2O_3. When the thickness of the highly conductive layer is <5 km, it is difficult to explain the electromagnetic coupling model using $CaIrO_3$ phase-bearing rock. However, the typical thickness of the D″ layer is 100–300 km. If the electrical conductivity of $CaIrO_3$-type $MgSiO_3$ is an order of magnitude higher than $MgSiO_3$ perovskite, then the electromagnetic coupling model is reasonable. This change in the electrical conductivity in $MgSiO_3$ is consistent with the observed change in Al_2O_3 [48]. This implies that the base of the lower mantle corresponding to the D″ layer may be a highly conductive layer. Thus, the exchange of angular momentum between the solid mantle and the fluid core by an electromagnetic core–mantle coupling may be the dominant mechanism for the observed change in the length of Earth's day on a decadal timescale. To discuss our quantitative analysis, it is necessary to perform direct measurements of the electrical conductivity of $CaIrO_3$-type $MgSiO_3$.

Based on the above, we estimated the profile of the electrical conductivity of the bottom of the lower mantle. Fig. 6 shows the estimated profile of the electrical conductivity. A marked change in the conductivity profile occurs, depending on the geotherm. According to the sandwich-structure (or double-crossing) model [49,50], the lowermost D″ layer does not consist of a post-perovskite-bearing rock. We have calculated two profiles of the electrical conductivity corresponding to hot and cold geotherms (Fig. 6a). When the temperature at the top of the outer core is lower than 4000 K, the D″ layer consists of only a post-perovskite-bearing rock. Thus, the discontinuity in electrical conductivity only occurs at the top of the D″ layer. In contrast, in this scenario, two discontinuities occur at both the top and the bottom of the D″ layer, when the temperature of the outer core is >4000 K, and a thin layer of low electrical conductivity should exist at the bottom of the D″ layer.

Acknowledgments

We thank Y. Ohishi and T. Kikegawa for help during synchrotron experiments. The synchrotron radiation experiments were performed at the SPring-8, JASRI (Proposal No. 2003A0013-LD2-np) and at the PF, KEK (Proposal No. 2003G187). Calculations were performed at CSCS (Manno) and ETH Zurich. This work was partially supported by the Ministry of Education, Culture, Sport, Science and Technology, Japan.

References

[1] F.C. Marton, R.E. Cohen, Prediction of a high-pressure phase transition in Al_2O_3, Am. Mineral. 79 (1994) 789–792.
[2] K.T. Thomson, R.M. Wentzcovitch, M.S.T. Bukowinski, Polymorphs of alumina predicted by first principles: putting pressure on the ruby pressure scale, Science 274 (1996) 1880–1882.
[3] N. Funamori, R. Jeanloz, High-pressure transformation of Al_2O_3, Science 278 (1997) 1109–1111.
[4] T. Mashimo, K. Tsumoto, K. Nakamura, Y. Noguchi, K. Fukuoka, Y. Syono, High-pressure phase transformation of corundum (α-Al_2O_3) observed under shock compression, Geophys. Res. Lett. 27 (2000) 2021–2024.
[5] J.F. Lin, O. Degtyareva, C.T. Prewitt, P. Dera, N. Sata, E. Gregoryanz, H.-K. Mao, R. Hemley, Crystal structure of a high-pressure/high-temperature phase of alumina by in situ X-ray diffraction, Nat. Mater. 3 (2004) 389–393.
[6] S. Jahn, P.A. Madden, M. Wilson, Dynamic simulation of pressure-driven phase transformation in crystalline Al_2O_3, Phys. Rev., B 69 (2004) 020106.
[7] W. Duan, R.M. Wentzcovitch, K.T. Thomson, First-principles study of high-pressure alumina polymorphs, Phys. Rev., B 57 (1998) 10363.
[8] A.R. Oganov, S. Ono, The high pressure phase of alumina and implications for Earth's D″ layer, Proc. Natl. Acad. Sci. 102 (2005) 10828–10831.
[9] R. Caracas, R.E. Cohen, Prediction of a new phase transition in Al_2O_3 at high pressures, Geophys. Res. Lett. 32 (2005) L06303.
[10] J. Tsuchiya, T. Tsuchiya, R.M. Wentzcovitch, Post-Rh_2O_3(II) transition and the high P,T phase diagram of alumina, Phys. Rev., B 72 (2005) 020103.
[11] R. Hide, J.O. Dickey, Earth's variable rotation, Science 253 (1991) 629–637.
[12] J. Bloxham, Dynamics of angular momentum in the Earth's core, Annu. Rev. Earth Planet. Sci. 26 (1998) 501–517.
[13] D. Jault, J.L. Le Mouël, The topographic torque associated with a tangentially geostrophic motion at the core surface and inferences on flow inside the core, Geophys. Astrophys. Fluid Dyn. 48 (1989) 273–296.
[14] B.A. Buffett, A mechanism for decade fluctuations in the length of day, Geophys. Res. Lett. 23 (1996) 3803–3806.
[15] R. Hide, The Earth's differential rotation, Q. J. R. Astron. Soc. 278 (1986) 3–14.
[16] D. Jault, J.L. Le Mouël, Exchange of angular momentum between the core and the mantle, J. Geomagn. Geoelectr. 43 (1991) 111–129.
[17] W. Kuang, J. Bloxham, On the dynamics of topographical core–mantle coupling, Phys. Earth Planet. Inter. 99 (1997) 289–294.

[18] M. Stix, P.H. Roberts, Time-dependent electromagnetic core–mantle coupling, Phys. Earth Planet. Inter. 36 (1984) 49–60.
[19] D.N. Stewart, F.H. Busse, K.A. Whaler, D. Gubbins, Geomagnetism, Earth rotation and the electrical conductivity of the lower mantle, Phys. Earth Planet. Inter. 92 (1995) 199–214.
[20] R. Holme, Electromagnetic core–mantle coupling, I, explaining decadal changes in the length of day, Geophys. J. Int. 132 (1998) 167–180.
[21] R. Holme, Electromagnetic core–mantle coupling: II. Probing deep mantle conductance, in: M. Gurnis, M.E. Wysession, E. Knittle, B.A. Buffett (Eds.), The Core–Mantle Boundary Region, AGU, 1998, pp. 139–151.
[22] J. Wicht, D. Jault, Electromagnetic core–mantle coupling for laterally varying mantle conductivity, J. Geophys. Res. 105 (2000) 23569–23578.
[23] T. Katsura, K. Sato, E. Ito, Electrical conductivity of silicate perovskite at lower-mantle conditions, Nature 395 (1998) 493–495.
[24] Y. Xu, C. McCammon, B.T. Poe, The effect of alumina on the electrical conductivity of silicate perovskite, Science 282 (1998) 922–924.
[25] J.-P. Poirier, J.-L. Le Mouël, Does infiltration of core material into the lower mantle affect the observed geomagnetic field? Phys. Earth Planet. Inter. 73 (1992) 29–37.
[26] B.A. Buffett, Constrants on magnetic energy and mantle conductivity from the forced nutations of the Earth, J. Geophys. Res. 97 (1992) 19581–19597.
[27] B.A. Buffett, E.J. Garnero, R. Jeanloz, Sediments at the top of Earth's core, Science 290 (2000) 1338–1342.
[28] A.R. Oganov, S. Ono, Theoretical and experimental evidence for a post-perovskite phase of $MgSiO_3$ in Earth's D″ layer, Nature 430 (2004) 445–448.
[29] T. Tsuchiya, J. Tsuchiya, K. Umemoto, R.M. Wentzcovitch, Phase transition in $MgSiO_3$ perovskite in the earth's lower mantle, Earth Planet. Sci. Lett. 224 (2004) 241–248.
[30] S. Ono, T. Kikegawa, Y. Ohishi, A high-pressure and high-temperature synthesis of platinum carbide, Solid State Commun. 133 (2005) 55–59.
[31] S. Ono, Y. Ohishi, M. Isshiki, T. Watanuki, In situ X-ray observations of phase assemblages in peridotite and basalt compositions at lower mantle conditions: implications for density of subducted oceanic plate, J. Geophys. Res. 110 (2005) B02208.
[32] G. Shen, M.L. Rivers, Y. Wang, S.R. Sutton, Laser heated diamond cell system at the Advanced Photon Source for in situ X-ray measurements at high pressure and temperature, Rev. Sci. Instrum. 72 (2001) 1273–1282.
[33] A. Kavner, W.R. Panero, Temperature gradients and evaluation of thermoelastic properties in the synchrotron-based laser-heated diamond cell, Phys. Earth Planet. Inter. 143–144 (2004) 527–539.
[34] S. Ono, K. Funakoshi, Y. Ohishi, E. Takahashi, In situ X-ray observation of phase transition between hematite–perovskite structures in Fe_2O_3, J. Phys., Condens. Matter 17 (2005) 269–276.
[35] S. Ono, K. Funakoshi, A. Nozawa, T. Kikegawa, High-pressure phase transitions in SnO_2, J. Appl. Phys. 97 (2005) 073523.
[36] A.P. Hammersley, S.O. Svensson, M. Hanfland, A.N. Fitch, D. Häusermann, Two-dimensinal detector software: from real detector to idealized image or two-theta scan, High Press. Res. 14 (1996) 235–245.
[37] J.C. Jamieson, J.N. Fritz, M.H. Manghnani, Pressure measurement at high temperature in X-ray diffraction studies: gold as a primary standard, in: S. Akimoto, M.H. Manghnani (Eds.), High-Pressure Research in Geophysics, Center for Academic Publishing, Tokyo, 1982, pp. 27–48.
[38] X. Gonze, J.-M. Beuken, R. Caracas, F. Detraux, M. Fuchs, G.-M. Rignanese, L. Sindic, M. Verstraete, G. Zerah, F. Jollet, M. Torrent, A. Roy, M. Mikami, P. Ghosez, J.-Y. Raty, D.C. Allan, First-principles computation of materials properties: the ABINIT software project, Comput. Mater. Sci. 25 (2002) 478–492.
[39] N. Troullier, J.L. Martins, Efficient pseudopotentials for plane-wave calculations, Phys. Rev., B 43 (1991) 1993–2006.
[40] S.G. Louie, S. Froyen, M.L. Cohen, Nonlinear ionic pseudopotentials in spin-density functional calculations, Phys. Rev., B 26 (1982) 1738–1742.
[41] S. Baroni, P. Gianozzi, A. Testa, Green-function approach to linear response in solids, Phys. Rev. Lett. 58 (1987) 1861–1864.
[42] X. Gonze, C. Lee, Dynamical matrices, born effective charges, dielectric permittivity tensors, and interatomic force constants from density-functional perturbation theory, Phys. Rev., B 55 (1997) 10355–10368.
[43] S. Baroni, S. de Gironcoli, A. Dal Corso, P. Gianozzi, Phonons and related crystal properties from density-functional perturbation theory, Rev. Mod. Phys. 73 (2001) 515–562.
[44] C.A. McCammon, Perovskite as a possible sink for ferric iron in the lower mantle, Nature 384 (1997) 694–696.
[45] D.J. Frost, C. Liebske, F. Langenhorst, C.A. McCammon, R.G. Trønnes, D. Rubie, Experimental evidence for the existence of iron-rich metal in the Earth's lower mantle, Nature 428 (2004) 409–412.
[46] B.J. Wood, D.C. Rubie, The effect of alumina on phase transformations at the 660-kilometer discontinuity from Fe–Mg partitioning experiments, Nature 273 (1996) 1522–1524.
[47] Y. Xu, T.J. Shankland, B.T. Poe, Laboratory-based electrical conductivity in the Earth's mantle, J. Geophys. Res. 105 (2000) 27865–27875.
[48] S.T. Weir, A.C. Mitchell, W.J. Nellis, Electrical resistivity of single-crystal Al_2O_3 shock-compressed in the pressure range 91–220 GPa (0.91–2.20 Mbar), J. Appl. Phys. 80 (1996) 1522–1525.
[49] J.W. Hernlund, C. Thomas, P.J. Tackley, A doubling of the post-perovskite phase boundary and structure of the Earth's lowermost mantle, Nature 434 (2005) 882–886.
[50] S. Ono, A.R. Oganov, In situ observations of phase transition between perovskite and $CaIrO_3$-type phase in $MgSiO_3$ and pyrolitic mantle composition, Earth Planet. Sci. Lett. 236 (2005) 914–932.
[51] Z. Hashin, S. Shtrikman, A variational approach to the theory of the effective magnetic permeability of multiphase materials, J. Appl. Phys. 33 (1962) 3125–3131.
[52] R. Landauer, The electrical resistance of binary metallic mixtures, J. Appl. Phys. 23 (1952) 779–784.